THE JOURNAL OF PHYSICAL CHEMISTRY C

ARTICLE

pubs.acs.org/JPCC

Understanding the Band Gap, Magnetism, and Kinetics of Graphene Nanostripes in Graphane

Liang Feng Huang,* Xiao Hong Zheng, Guo Ren Zhang, Long Long Li, and Zhi Zeng*

Key Laboratory of Materials Physics, Institute of Solid State Physics, Chinese Academy of Sciences, Hefei 230031, People's Republic of China

Supporting Information

ABSTRACT: The electronic structure and kinetic stability of various graphene nanostripes (GNSs) in graphane are systematically studied by ab initio simulations. The band gap of armchair GNS (nonmagnetic) is determined by the quantum confinement of π electrons and modified by the contraction of the edge C−C bonds. The band gap of zigzag GNS is induced by the exchange splitting of the edge states and its magnetism closely correlates with the long-range nature of π electrons, quantum confinement, intraedge exchange interaction, and interedge superexchange interaction. The kinetic stability of these GNSs in graphane is probed by the potential barriers and reaction rates for the diffusion and desorption of the hydrogen adatoms at various graphene/graphane interfaces. These interfaces are very stable under conventional thermalization conditions. The conformation of graphane has a small effect on the electronic structure of GNS but has a significant effect on the kinetic stability of the interfacial adatoms. The hydrogen adatoms in the graphane bulk are much more stable than the interfacial ones, which implies the possibility to carve out sharp-edge GNSs in graphane. An approach is proposed to fabricate integrated field-effect transistors based on sharp-edge and substrate-decoupled GNSs in substrate-supported graphane.

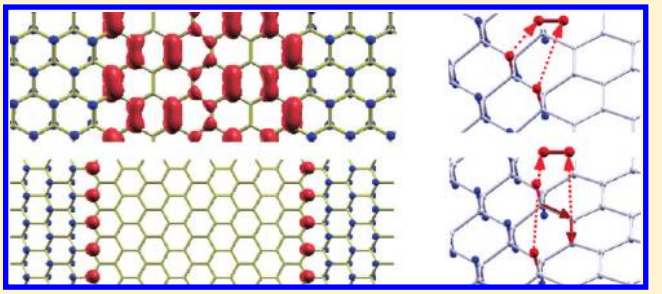

INTRODUCTION

Graphene is an atomically thick carbon (sp^2-hybridized) layer and is a promising material in the field of nanotechnology due to its low mass density, high carrier mobility, superior mechanical properties, and controllable synthesis.[1−7] However, pristine graphene is semimetallic and a band gap is required when using it for field-effect transistors (FET).[4]

Graphane is fully two-side hydrogenated graphene with all the carbon atoms in the sp^3 hybridized state,[8−10] which is a wide-band-gap (>3.2 eV) insulator.[10−13] Thus, the low-energy carriers in a graphene nanostripe (GNS) carved in graphane (see Figure 1 for the structure, also called nanoroad by Singh[14]) can be effectively confined by the two graphene/graphane interfaces. Even couples of adatom lines can dehybridize two neighboring GNSs.[15−18] Although there is a lattice mismatch between graphene and graphane,[19] the intrinsic rippling of the flexible graphene−graphane composite sheet will release the internal stress.[20] Chirality and width-dependent band gap and magnetism have been theoretically observed in GNS,[14,17,21,22] and clear understanding of the mechanism is a prerequisite of its application in FETs and spintronic devices. The quantum confinement and the edge imperfection make GNS a perfect counterpart of a graphene nanoribbon (GNR), which has been widely studied by experimentalists and theorists.[23−38] The only difference between these two counterparts is the status of the edge, either supported by graphane or free in vacuum. Studies on the band gap and magnetism of GNS in graphane will not only reveal its electronic properties but also bring some important underneath mechanisms to light when compared to the results of GNR. Furthermore, according to Flores's molecular-dynamics simulations,[39] disordered conformation of graphane should be favored after realistic hydrogenation, although the chair conformation has been found to be the most stable periodic conformation.[10] Thus, understanding the conformation effect on the electronic properties of GNS is especially meaningful for further investigation and realistic application.

Experimentalists have made a breakthrough to carve out GNSs in one-side hydrogenated graphene via electron-stimulated hydrogen desorption,[40] although the interfaces are still smeared there. Such interfacial smearing is probably caused by the one-side hydrogenation. Because, it has been found that, during the one-side hydrogenation, the hydrogen coverage is limited by both the increase of the elastic energy of the carbon lattice and the abstraction of the adatoms by the incident atoms.[41−46] Furthermore, according to the thermal desorption spectra of the hydrogen adatoms on one side of graphene,[41,43,47] the kinetic stability of the adatoms is not significantly enhanced when increasing the coverage up to the saturation coverage (∼28% for H; ∼35% for D). Consequently, when carving GNSs in one-side hydrogenated graphene, there is no significant stability difference between the adatoms at the GNS edges and those in the hydrogenated areas, resulting in smeared GNS edges. However, during the two-side hydrogenation of graphene, the adatoms at one side cannot be

Received: August 22, 2011
Revised: September 14, 2011
Published: September 20, 2011

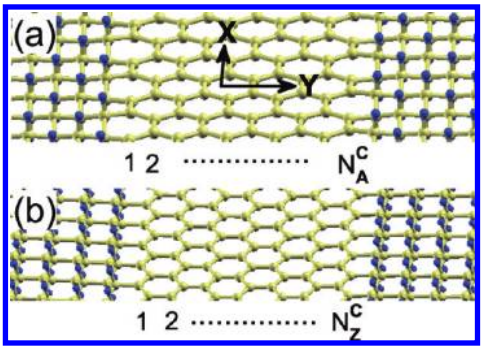

Figure 1. The structures of (a) Arm-GNS and (b) Zig-GNS in graphane. More details on the structures of various GNSs for electronic and kinetic simulations can be found in the Supporting Information.

abstracted out by the incident atoms onto another side, and the deformation of the carbon lattice is alleviated by the alternating puckering of carbon atoms. Thus, high adatom coverage can be obtained with the two-side hydrogenation.[9] The usability of graphane and the obtainability of sharp-edge GNSs in it heavily rely on the kinetic stability of the hydrogen adatoms, the understanding on which still lacks.

In this work, the band gap, magnetism, and kinetic stability of armchair GNS (Arm-GNS) and zigzag GNS (Zig-GNS) in graphane are studied by ab initio simulations. The effects of the graphane conformation, spatial confinement, edge-bond contraction, the intraedge exchange interaction, and the interedge superexchange interaction on the electronic structures of these GNSs are systematically inspected. The diffusion and desorption of the hydrogen adatoms at various graphene/graphane interfaces are studied with the potential barriers and reaction rates. The results indicate that it is possible to carve out sharp-edge GNSs in graphane. Finally, an approach is proposed to prepare integrated GNS-FETs with high quality on semiconductor substrate.

COMPUTATIONAL METHOD

The density-functional calculations of the structures, electronic structures, and vibrational frequencies are performed by the Quantum ESPRESSO code.[48] The relaxed periodic supercells and the corresponding *k*-point grids for the electronic and kinetic simulations of various GNSs in graphane are shown in the Supporting Information (Figures S1−S5). The distance between neighboring slabs (along the *z* direction) is set to be 12.0 Å. The electronic exchange-correlation interaction is described by the ultrasoft[49] PBE[50] pseudopotential. The energy cutoffs for wave function and charge density are 35 and 350 Ry, respectively. The supercell lattice constants in the *XY* plane and the internal atomic positions are fully relaxed with a pressure threshold of 0.1 GPa and force threshold of 10^{-4} Ry/bohr, respectively. The reaction paths are searched using the climbing-image nudged elastic band method.[51] The reaction rates of the diffusion and desorption of the interfacial hydrogen adatoms are calculated using quantum mechanically modified transition state theory.[52]

The widths of Arm-GNS (W_A) and Zig-GNS (W_Z) are measured by the number of the sp^2-hybridized carbon dimer lines (N_A^C, $W_A \approx 1.23 \times N_A^C$ Å), and zigzag chains (N_Z^C, $W_Z \approx 2.13 \times N_Z^C$ Å), respectively (Figure 1). The total number of carbon dimer lines or zigzag chains (N_{tot}) of a periodic supercell measures its size. In the electronic simulations, two sets of supercells (N_{tot} = 20 and 26 for Arm-GNS or N_{tot} = 16 and 26 for Zig-GNS) are used to accommodate GNSs of different sizes. We will show that the numerical mismatch between these two groups is very small. The electronic exchange and correlation interaction are described by the PBE potential[50] in this work, which is effective and efficient in qualitatively investigating the electronic structure of confined graphene systems, although conventional density functionals always quantitatively underestimate the band gap.[33,34,53] This underestimation of the band gap could be attributed to the overestimation of the electronic screening of the excited states by conventional density functionals,[53−55] which should not affect the qualitative exploration of the electronic-interaction mechanism in this work.

RESULTS AND DISCUSSION

Arm-GNS is nonmagnetic and has a direct band gap (E_g) at the Γ point (Figure 2a). The wave functions (or charge densities) of the conduction-band-minimum (CBMin) and valence-band-maximum (VBMax) states distribute quite uniformly across Arm-GNS. E_g oscillatingly decreases with increasing N_A^C (Figure 2b), which can be divided into three families, $E_g(3p)$ ($N_A^C = 3p$, p is integer), $E_g(3p + 1)$, and $E_g(3p + 2)$.[14,30] The graphane conformation (chair or boat) only has a small effect on these E_g values. The Arm-GNS (also the Zig-GNS) is more or less rippled by the interfaces (Figures S1 and S2 in the Supporting Information), and such rippling is dependent on the graphane conformation and the width. However, the electronic properties of GNS are mainly determined by the lateral size of the sp^2-carbon plane. Thus, the disorder in the conformation of the realistic graphane will not significantly affect the electronic properties of the carved GNSs. We could summarize the width dependence of the E_g in each family with an inverse function

$$E_g = \frac{\alpha}{N_A^C + \beta} \quad (1)$$

where α (in eV) and β (dimensionless) are fitting parameters. Such E_g relation follows its quantum-confinement origin, where the effective confinement width of the electrons in Arm-GNS is $1.23 \times (N_A^C + \beta)$ (Å). The fitted α and β values for each family of Arm-GNS are listed in Table 1. The magnitude order between these three families of E_g values is $E_g(3p + 1) > E_g(3p) > E_g(3p + 2)$, keeping the same order as that of Arm-GNR.[30,34]

The previous investigation has pointed out that the contraction of the edge C−C bonds results in the finite band gap of $(3p + 2)$-Arm-GNR.[30,35] We also find the contraction of the edge C−C bonds leading to the finite band gap of $(3p + 2)$-Arm-GNS, as seen from Figure 2c. Evidently, GNS provides another realistic system to dig out the understanding on the bond-contraction effect. The edge-bond contraction of Arm-GNS ($\lesssim$0.8%) is less than that of Arm-GNR (~4.0%[30]), which results in that the $E_g(3p + 2)$ of Arm-GNS is 0.1−0.4 eV less than that of Arm-GNR[30,34] within the considered width range here. Furthermore, this bond contraction of the Arm-GNS in chair graphane (~0.4%) is less than that in boat graphane (~0.8%); thus the $E_g(3p + 2)$ of the former is smaller than that of the latter (Figure 2b). The bond-contraction effect also decreases (increases) $E_g(3p)$ ($E_g(3p + 1)$),[30] thus the $E_g(3p)$ ($E_g(3p + 1)$) of the Arm-GNS in chair graphane is a little larger (smaller) than that in boat

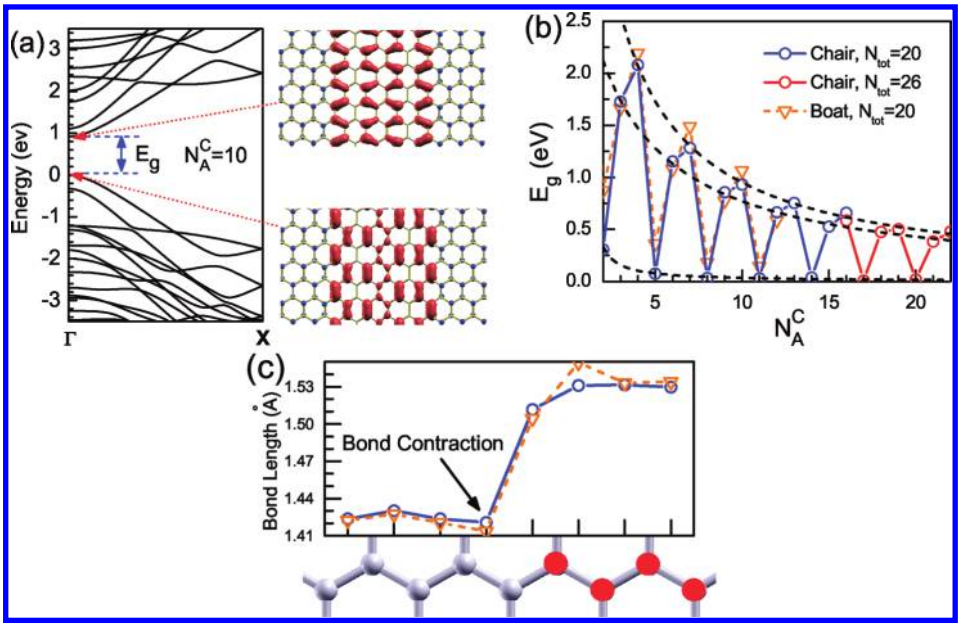

Figure 2. (a) The band structure of 10-Arm-GNS (left), together with the charge density of the CBMin and VBMax states (right). (b) The width dependence of the energetic band gap (E_g) of Arm-GNS. The black dashed lines are the fittings to the DFT calculations. (c) The site dependence of the C−C bond length at the Arm-graphene/graphane interface, where the hydrogenated C atoms are labeled by red circles.

Table 1. Fitted Parameters for the Width Dependence of the Band Gap of Arm-GNS

family	$3p$	$3p + 1$	$3p + 2$
α	9.7	10.5	0.3
β	2.6	1.1	−1.1

graphane (Figure 2b). It should be noted that the edge-bond contraction of Arm-GNS only results in small modifications to E_g, for that it is mainly determined by the width, as described by eq 1.

Different from the CBMin and VBMax states in Arm-GNS, localized states appear at the edges of Zig-GNS (Figure 3 panels a, b, and c), which is the same for Zig-GNR.[6,30,31,56,57] The nonmagnetic (NM) state of Zig-GNS is semimetallic (Figure 3c), with dispersionless degenerate bands at the Fermi level. This degeneracy makes the π electrons unstable in NM-Zig-GNS, and the spin polarization of the edges stabilizes this electron system.[58] The magnetism in Zig-GNS complicates the band structures, whereas we could use simple theoretical models to reveal the underlying mechanisms in the following. In the antiferromagnetic (AFM) and ferromagnetic (FM) states, the interedge magnetic moments are antiferromagnetically and ferromagnetically coupled, respectively, while the magnetic moments along each edge are ferromagnetically aligned with high spin-wave stiffness.[59] In FM-Zig-GNS, the symmetrical distribution of the charge density of each localized state (Figure 3b, right) can be understood from the wave function rearrangement induced by the quantum tunneling of electrons.[60] Because of the long-range screening of the π electrons in graphene,[61] the electronic response (charge density distribution, electronic interactions, etc.) to an imperfection always exhibits a power-law decay with distance ($\sim 1/r^m$)).[58,62−64] The mesomeric effect (resonating effect) in graphene systems[64,65] is also a reflection of this long-range nature. Thus, the covalent interaction between the edge-state tails also obeys a power-law decay, and the variation of the edge magnetic moment (M_{edge}) in Figure 3d is well fitted by

$$M_{edge}(N_Z^C) = 0.315 - \frac{50.0}{(N_Z^C + 5.94)^{2.73}} \quad (2)$$

The M_{edge} of a FM-Zig-GNS is nearly the same as that of a AFM-Zig-GNS (difference < $(1/10)M_{edge}$). For convenience and without loss of accuracy, the M_{edge} of FM-Zig-GNS (half of the total magnetic moment) is used here as the edge magnetic moment for both AFM- and FM-Zig-GNSs. The saturation value ($0.315\,\mu_B$) is close to the predicted value ($(1/3)\mu_B$) based on the mesomeric effect.[65]

The AFM and FM states are semiconductive and half-metallic, respectively (Figure 3a,b). The energy splitting between the valence and conduction bands at the X point (Brillouin zone boundary) in both AFM- (E_g^X) and FM-Zig-GNS (Δ_{FM}^X) is caused by the intraedge electronic exchange interaction, which is similar to the exchange splitting of the quasi-localized states in monohydrogenated graphene.[54] This intraedge exchange splitting is described by a simple exchange model[54]

$$E_{split}(N_Z^C) = J_{intra}(N_Z^C) \cdot M_{edge}(N_Z^C) \quad (3)$$

where E_{split} is E_g^X or Δ_{FM}^X; J_{intra} is the effective intraedge exchange constant. The variation of the J_{intra} for AFM- and FM-Zig-GNS (Figure 3e and f) is fitted to be

$$J_{intra}^{AFM}(N_Z^C) = 2.77 + \frac{23.3}{(N_Z^C + 1.60)^{1.78}} \quad (4)$$

and

$$J_{intra}^{FM}(N_Z^C) = 2.72 + \frac{783}{(N_Z^C + 11.4)^{2.60}} \quad (5)$$

dx.doi.org/10.1021/jp208067y |J. Phys. Chem. C 2011, 115, 21088–21097

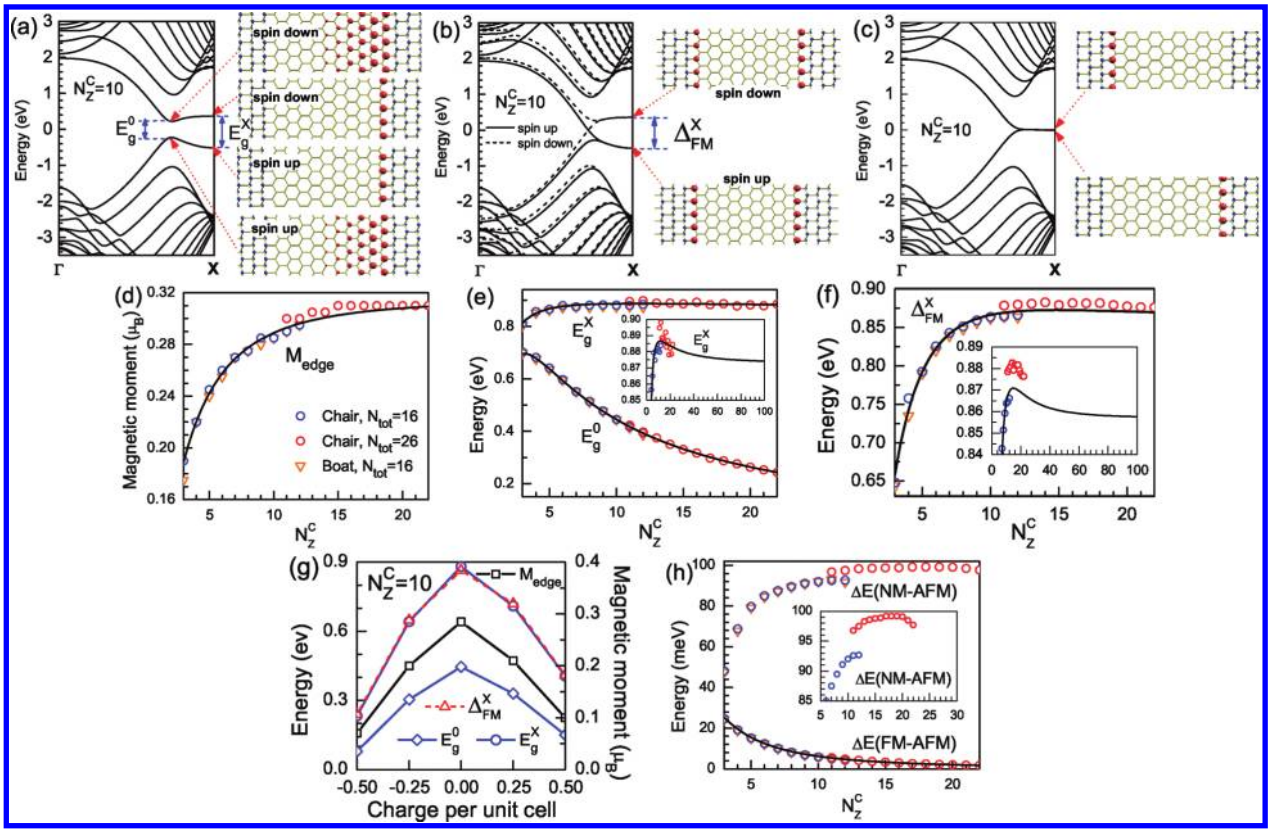

Figure 3. (a−c) The band structures (left) of 10-Zig-GNS in the AFM, FM, and NM states, together with the charge density of their edge states (right). The charge density of the left-edge states of AFM-Zig-GNS (not shown) is the reflection (about the GNS center) of those of the right-edge states in (a), but with the spin flipped for each state. (d−f) The width dependence of the edge magnetic moment (M_{edge}) and energetic band gaps (E_g^0, E_g^X, and Δ_{FM}^X, as labeled in (a) and (b)). (g) The doping-charge dependence of E_g^0, E_g^X, Δ_{FM}^X, and M_{edge} of 10-Zig-GNS. (h) The width dependence of the energies of the FM and NM states with respect to the AFM state, $\Delta E(\mathrm{FM}-\mathrm{AFM})$ and $\Delta E(\mathrm{NM}-\mathrm{AFM})$. The black lines in (d−f) and (h) are the fittings to the DFT calculations.

where the asymptotical power-law decay with width is due to the long-range nature of the π electrons, because a long-rang-decaying wave function has a smaller exchange integral in a wider Zig-GNS. E_g^X (Δ_{FM}^X) first increases with N_Z^C until a maximum of 0.887 (0.871) eV at N_Z^C = 12 (14), then decreases asymptotically down to 0.873 (0.855) eV (the insets in Figure 3 panels e and f). This peaked profile is caused conjunctly by the asymptotical decrease of J_{intra} (eq 4 and eq 5) and the asymptotical increase of M_{edge} (eq 2) with increasing N_Z^C. When k goes from the Γ point to the X point, the conduction and valence bands approach each other, while at the same time, the intraedge exchange splitting increases due to the enhanced localization of the wave function (Figure 3a, right). These two reverse effects conjunctly result in the appearance of the CBMin and VBMax states at $k = k_0$ ($(2/3)k_X < k_0 < k_X$) in the band structure of AFM-Zig-GNS (Figure 3a). In particular, the latter effect results in the increased energy shift between the spin-up and spin-down states of FM-Zig-GNS (Figure 3b). At any k point away from the X point, the conduction and valence bands get closer to each other in wider GNS than that in narrower GNS (Figure S6a and b in the Supporting Information), which is due to the quantum confinement effect. This makes the intraedge exchange interaction start to pull these two bands away from each other at a smaller k_0 in a wider GNS, and the value of k_0/k_X asymptotically decreases down to 0.67 with increasing N_Z^C (Figure S6c in the Supporting Information). Thus, both the confinement effect and the exchange splitting should contribute to the minimum band gap at k_0 (E_g^0), which is described by a relation with two decay powers

$$E_g^0(N_Z^C) = \frac{6.15}{N_Z^C + 2.08} - \frac{23.1}{(N_Z^C + 1.98)^{2.37}} \quad (6)$$

which well fits the calculated variation of E_g^0 (Figure 3e). The first term determines E_g^0, especially in wide GNSs. E_g^0 decreases asymptotically down to zero, because the charge density of the CBMin and VBMax states distribute quasi-locally at one-half of Zig-GNS (Figure 3a), and the confinement effect and exchange splitting of them are expected to diminish in very wide Zig-GNSs.

The intraedge exchange interaction resides in E_g^X, E_g^0, and Δ_{FM}^X also indicates that these band gaps will decrease upon electron or hole doping, which is verified by our DFT calculations as shown in Figure 3g. Because electron doping of Zig-GNS makes the conduction band occupied, while hole doping reduces the occupation number of the valence band, both of which decrease the spin polarization of each edge (M_{edge}), and then reduce the exchange splitting between these two bands (by eq 3). $J_{intra}^{AFM/FM}$ nearly keep constant under doping. The decrease of E_g^0 with increasing the width or the doping charges of Zig-GNS in this work is consistent with a recent experimental measurement on GNRs with small chiral angles (close to the zigzag chirality).[66] This kind of M_{edge}-dependent exchange splitting is expected to play an important role in the half-metallicity mechanism of the

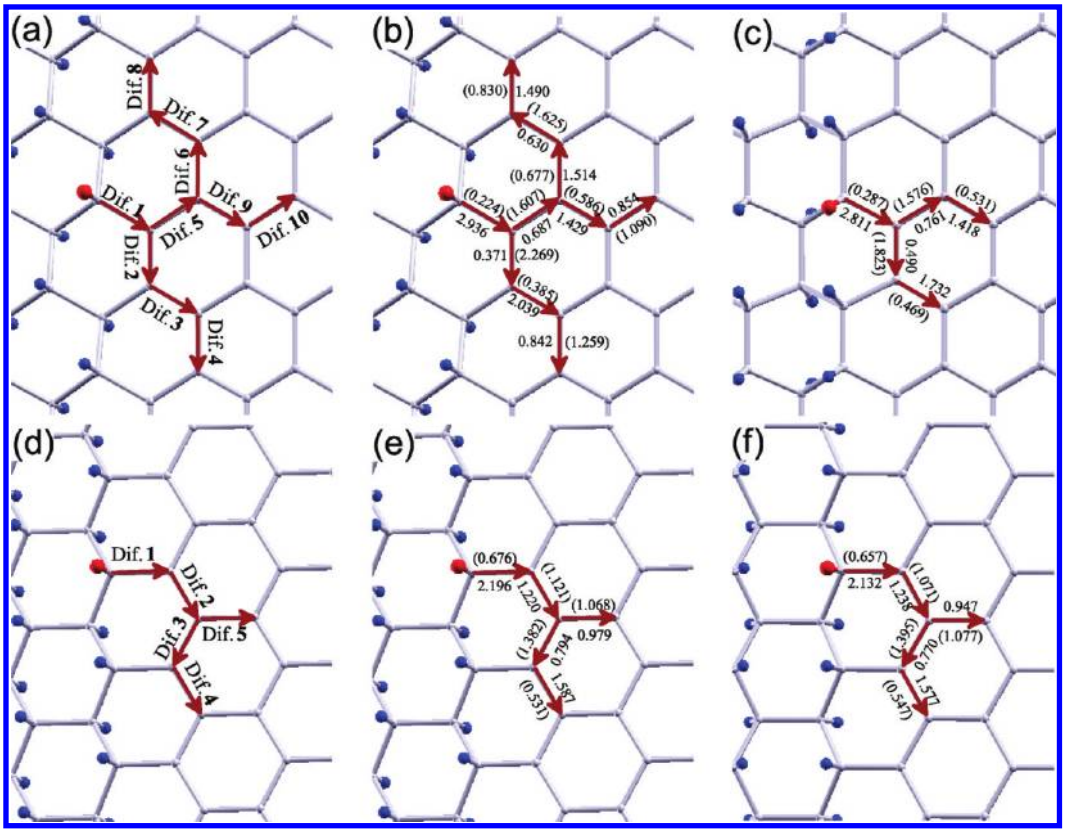

Figure 4. (a, d) Labeled diffusion paths for a H adatom (in red) at the Arm- and Zig-graphene/graphane interfaces. The potential barriers (in eV) for the diffusion of a H adatom at the (b) Arm-graphene/graphane(chair), (c) Arm-graphene/graphane(boat), (e) Zig-graphene/graphane(chair), and (f) Zig-graphene/graphane(boat) interfaces. The barriers for the diffusion paths reverse to the arrows are shown in parentheses.

GNRs with edge substituents (boron and nitrogen atoms)[67−69] or the GNRs under transverse electric field,[31,70,71] where the electronic occupations of the two edges are unequal.

The width dependence of the energies of the FM and NM states with respect to the AFM state, $\Delta E(\mathrm{FM}-\mathrm{AFM})$ and $\Delta E(\mathrm{NM}-\mathrm{AFM})$, are both shown in Figure 3h. The AFM state is more stable than the FM state at 0 K, due to the interedge superexchange interaction[6] with a negative effective exchange constant (J_{inter}). A simple Heisenberg model could describe this interedge interaction

$$\Delta E(\mathrm{FM}-\mathrm{AFM}) = -J_{\mathrm{inter}} \cdot (M_{\mathrm{edge}})^2 \quad (7)$$

where J_{inter} is fitted to be

$$J_{\mathrm{inter}}(N_Z^{\mathrm{C}}) = -\frac{3565}{(N_Z^{\mathrm{C}}-0.416)^{1.72}} \quad (8)$$

where the power-law decay of J_{inter} also comes from the long-range nature of the π electrons. $\Delta E(\mathrm{NM}-\mathrm{AFM})$ is related to the excitation of the electrons from the ground state (AFM); thus, it is dependent on the band gap between the conduction and valence bands of AFM-Zig-GNS. Although the variation of $\Delta E(\mathrm{NM}-\mathrm{AFM})$ resembles that of E_{g}^X to some extent, and also presents a peaked profile with a maximum of 99.2 meV at $N_Z^{\mathrm{C}} = 18$, it cannot be simply fitted by any weighted average of E_{g}^X and E_{g}^0. This is because much more than two channels of electronic excitation should be responsible for the value and variation of $\Delta E(\mathrm{NM}-\mathrm{AFM})$, and the contributions of confinement effect and intraedge exchange splitting to these channels vary a lot. Considering the thermalization at finite temperatures (e.g., 300 K, 26 meV), Zig-GNS is expected to be in a paramagnetic phase without external fields. This is because under conventional thermalization, the FM and AFM states could be degenerate due to the small $\Delta E(\mathrm{FM}-\mathrm{AFM})$, while the spin polarization of each edge could survive due to the relative large $\Delta E(\mathrm{NM}-\mathrm{AFM})$. There exists an optimal Zig-GNS width of 38 Å ($N_Z^{\mathrm{C}} = 18$) for the magnetic stability of the edges.

The above analysis on the electronic properties of the GNSs carved in graphane shows that there exist many degrees of freedom (chirality, width and edge occupation) to modulate their band gaps and magnetism, which indicates their promising application in nanodevices. However, the usability of GNS still relies on its obtainability and structural stability, both of which are closely related with the kinetic properties (diffusion and desorption) of the hydrogen adatoms at the graphene/graphane interface.

The probability of disorder in the conformation of graphane[39] impels us to explore the kinetic stability of various graphene/graphane interfaces, armchair and zigzag interfaces with graphane in the chair or boat conformation. Various possible reaction paths and their potential barriers for the diffusion of a H adatom from these interfaces are shown in Figure 4, and those for the (diffusion-assisted) desorption of a H_2 molecule from these interfaces are shown in Figure 5 and Figure 6. The physisorption energy of a H_2 molecule at the top of the interface is just about 10 meV, which can be safely neglected in our discussion. The diffusion paths are labeled by numbers (e.g., Dif.1), and the desorption paths are labeled by numbers together with the configuration of the H dimer before desorption (e.g., Des.M1), where P, O, and M

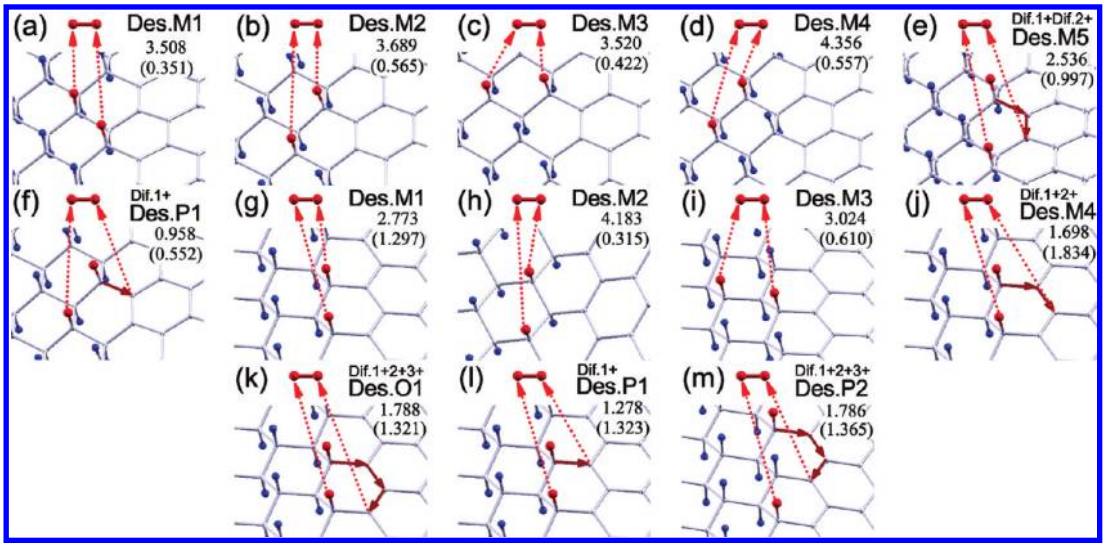

Figure 5. The potential barriers (in eV) for the direct and diffusion-assisted desorption of a H_2 molecule (in red) from the (a−f) Arm-graphene/graphane(chair) and (g−m) Zig-graphene/graphane(chair) interfaces. The values of the adsorption barriers are shown in parentheses.

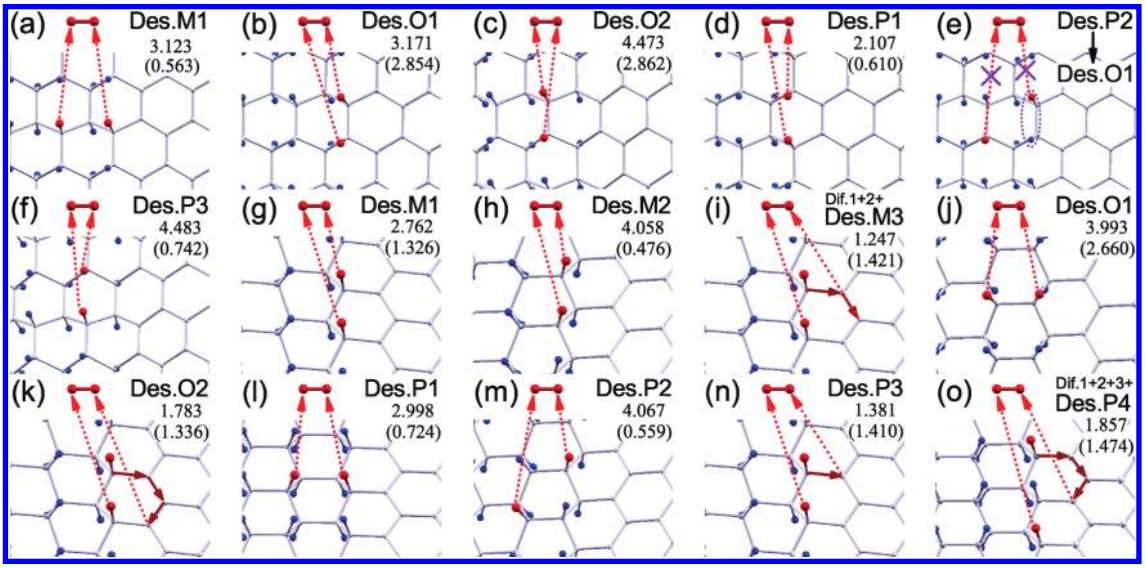

Figure 6. The potential barriers (in eV) for the direct and diffusion-assisted desorption of a H_2 molecule from the (a−f) Arm-graphene/graphane(boat) and (g−o) Zig-graphene/graphane(boat) interfaces. The Des.P2 path in (e) is not stable in simulation and transforms into the Des.O1 path in (b). The values of the adsorption barriers are shown in parentheses.

represent the para-, ortho-, and meta-dimer configurations, respectively. The interface chirality (armchair or zigzag) significantly influences the diffusion potential barriers, while the graphane conformation (chair or boat) does not, except for some minor influence on the values. The potential barrier for the first-step diffusion (Dif.1) is about 2.874 (2.164) eV for the Arm-graphene/graphane (Zig-graphene/graphane) interface, while the barrier for the diffusion path reverse to Dif.1 (Dif.$\bar{1}$) is much lower, about 0.256 (0.667) eV. The barriers for other diffusion paths and their reverses are also much lower than that of Dif.1, from 0.371 (0.531) to 2.269 (1.587) eV for Arm- (Zig-) interface. These relative magnitudes of potential barriers indicate that the H adatoms much favor to stay at the graphene/graphane interface, which is consistent with other results.[72,73] This is because the sp^3-hybridized C atoms, which is well indicated by the average ∠CCC of the vertex C atoms (Figure 7), are much more reactive than the sp^2-hybridized ones to bond with H atoms.[74,75] This law on the adsorption stability of hydrogen is also reflected in the desorption barriers, and we can take the Zig-graphene/graphane(chair) interface (Figure 5g−m) as the demonstration example. The desorption of a H_2 molecule from the bulk of graphane in chair (boat) conformation must overcome a potential barrier of 4.352 (3.936) eV. If the two H atoms are both in graphane at the Zig-graphene/graphane(chair) interface (Des.M2 in Figure 5h), the desorption barrier is 4.183 eV, which is close to that for the desorption from bulk graphane (4.352 eV). If only one H atom is in graphane and the other one is in the graphane front of the interface (Des.M3 in Figure 5i), the barrier is lowered to be 3.024 eV. If the two H atoms are both in the graphane front (Des.M1 in Figure 5g), the barrier is further lowered to be 2.773 eV. In the

diffusion-assisted desorption situations (Figure 5j−m), where one H atom is in the graphane front and the other one is adsorbed on graphene, all the desorption barriers are lower than 1.800 eV. Such location (or sp^3-hybridization) dependence of desorption barrier also holds for all the Arm-graphene/graphane-(chair) (Figure 5a−f), Arm- (Figure 6a−f) and Zig-graphene/graphane(boat) interfaces (Figure 6g−o). It indicates that the desorption of H adatoms will start at the interfaces when the system is placed under thermalization or other kinds of excitation. Furthermore, the desorption barrier is also related with the H-dimer configuration, which is determined by both the interface chirality and graphane conformation. Comparing all the potential barriers for diffusion and desorption in Figure 4, Figure 5, and Figure 6, if a H adatom succeeds in Dif.1, it will either immediately diffuse back into the interface or quickly combine with another interfacial H adatom to form a desorbed H_2 molecule through the diffusion-assisted desorption. The adsorption barriers, varying from 0.351 to 2.862 eV, tend to make the desorbing H_2 molecule gain high escaping velocity (0.1 eV ∼ 3000 m/s), vibrational and rotational speeds after climbing over the desorption barrier.

The lattice mismatch between graphene and graphane readily causes intrinsic rippling in the flexible graphene−graphane composite sheet,[19,20] which does not appear in our DFT simulations because of the small size and periodicity of the structural models used here. However, the rippling is smooth and the dimension ranges from 40 to 80 Å,[20] which should not significantly influence the local curvature of the carbon lattice at the atomic scale and not affect the reaction paths and barriers predicted above. This can be shown by comparing the diffusion barriers for a H adatom at the graphene/graphane(chair) and graphene/graphane(boat) interfaces. Although these two types of interfaces have small difference in the lattice curvature (Figure S4 and S5 in the Supporting Information), the diffusion barriers for a H adatom at these two interfaces are very close to each (Figure 4).

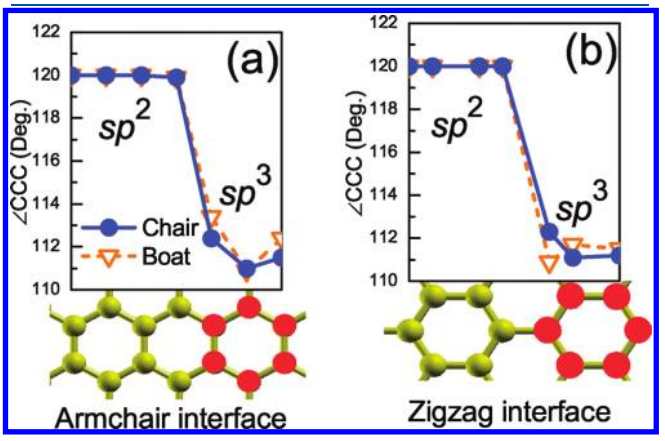

Figure 7. The site dependence of the average ∠CCC angle of the vertex C atom, where the hydrogenated C atoms are labeled by red circles.

In order to further understand the kinetic stability of H adatoms at the graphene/graphane interface, thermal desorption rates (jump frequencies) of the interfacial H adatoms along various paths are calculated using quantum-mechanically modified transition state theory.[52] The chosen paths are expected, according to the potential-barrier values, to be the most possible reaction paths for the direct or diffusion-assisted desorption. The formulas for the jump frequencies (ν) of these one-step and multistep paths, as well as the zero-point energy corrections to the potential barriers, are presented in the Supporting Information. Except at the Arm-graphene/graphane(boat) interface, the jump frequencies of the direct and diffusion-assisted desorption of the interfacial H adatoms are close to each other (within 1 order of magnitude) (Figure 8 panels a, b, and d). For the Arm-graphene/graphane-(boat) interface, the path Des.P1 has much lower potential barrier (2.107 eV, Figure 6d) than that of Dif.1 (2.811 eV, Figure 4c); thus ν(Des.P1) is much larger than ν(Dif.1) (Figure 8c), and the diffusion-assisted desorption will not occur at this interface. Thus, the reaction rate of a desorption path is dependent on the interface chirality, graphane conformation, and predesorption H-dimer configuration. The H adatoms at realistic graphene/graphane interfaces should be desorbed directly into vacuum or diffuses into graphene, which is quickly followed by the combination with other interfacial adatoms into desorbed H_2 molecules. If graphene is not 100% hydrogenated, the adatoms tend to form clusters due to the effective attraction between them,[47] and the kinetic stability of the H adatoms is measured by the lifetime ($\tau \sim 1/\nu$) of the interfacial adatoms. At 300 K, the lifetimes of the interfacial H adatoms are 4.5×10^{39}, 4.2×10^{28}, 9.1×10^{17}, and 8.3×10^{27} s for the Arm-graphene/graphane(chair), Zig-graphene/graphane(chair), Arm-graphene/graphane(boat), and Zig-graphene/graphane(boat) interfaces, respectively, and at 723 K, their lifetimes are 1.1×10^{8}, 1.4×10^{3}, 3.3×10^{-1}, and 2.8×10^{3} s, respectively. This is qualitatively consistent with the experimental measurement on realistic graphane, which is stable for many days at room temperature and totally dehydrogenated at 723 K within 24 h ($\tau < 8.6 \times 10^{4}$ s).[9] All kinds of

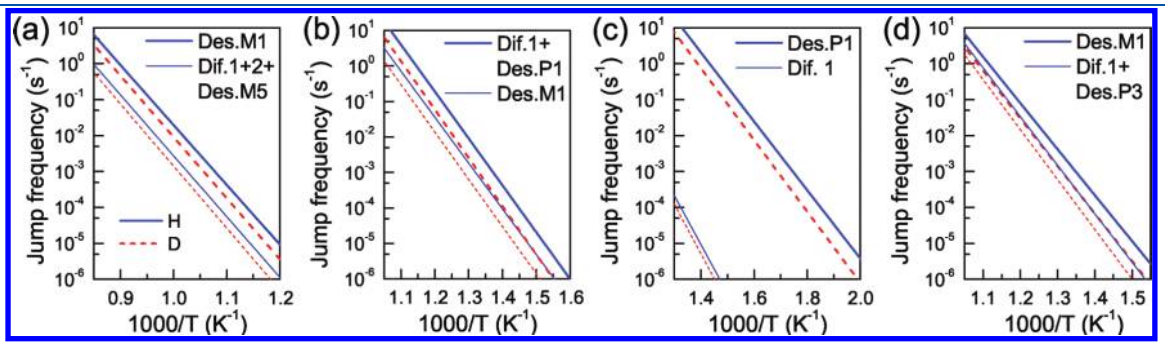

Figure 8. The temperature dependence of the jump frequencies for the direct and diffusion-assisted desorption of a H_2 molecule from the (a) Arm-graphene/graphane(chair), (b) Zig-graphene/graphane(chair), (c) Arm-graphene/graphane(boat), and (d) Zig-graphene/graphane(boat) interfaces. In (c), the jump frequency (ν) of the diffusion-assisted desorption is neglected because ν(Dif.1) is very small compared with ν(Des.P1). The isotope effect is shown by replacing hydrogen by deuterium.

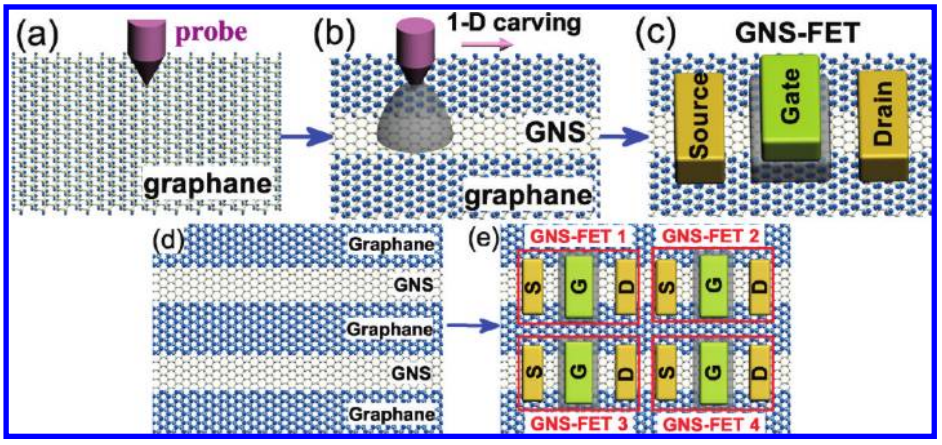

Figure 9. (a−c) Schematic drawing of the preparation steps of a GNS-FET (top-gated). (a) A probe approaches a graphane surface supported by a semiconductor substrate (not shown). (b) A one-dimension GNS is carved out via the electron-current-excited desorption of the H adatoms. The H adatoms desorbed downward tend to be adsorbed onto the semiconductor substrate, which will prevent the GNS from covalently bonding with the substrate. (c) A GNS-FET is obtained after depositing the source and drain electrodes, dielectrics, and the gate electrode, consecutively. (d, e) The preparation of integrated GNS-FETs from integrated GNSs in graphane.

interfaces are probably present in the realistic graphane. If deuterium replaces hydrogen, τ increases by more than 0.5 times. In a quick fabrication of GNS in graphane, a short adatom lifetime (<0.1 s) is always required, which needs a high (effective) temperature (>1100 K) (Figure 8).

The high stability of the graphene/graphane interfaces at room temperature indicates the usability of GNS-based devices under conventional thermalization conditions, and the fact that the adatoms in the graphane bulk are much more stable than the interfacial ones implies the possibility to carve out sharp-edge GNS in graphane. Scanning probe microscope (SPM) lithography is a well-developed approach to prepare nanostructures on surfaces,[76,77] and has been used to carve out graphene nanodots and nanostripes in one-side hydrogenated graphene on a SiC surface.[40] We thus propose to use this method to integrate GNSs in graphane. Before the lithography processing, graphane should be transferred onto a substrate after the hydrogenation of suspended graphene, or even two-side hydrogenation of graphene directly on substrate is also possible.[78] In SPM lithography, the electron-current excitation and the probe interaction serve as effective local thermalization and catalysis, respectively.[77,79] The desorption barriers of the interfacial H adatoms only change by about 0.1 eV even though an electric field as high as 10^9 V/m is applied in our DFT simulations, which should be due to the low electric polarizability of hydrogenated graphene.[80] Thus, the electric field alone is not enough, and instead the electron-current excitation, which is responsible for the breaking of the C−H bonds on diamond surfaces,[76] is critical to the fabrication of GNSs in graphane. The proposed steps for the preparation of integrated GNS-based FETs (GNS-FET) in graphane (supported by a semiconductor substrate) are shown in Figure 9. The H_2 molecules desorbed upward from graphane will escape into vacuum with high velocity, while those desorbed downward tend to dissociate again and be adsorbed onto the semiconductor substrate.[81−84] These adsorbed H adatoms on the substrate beneath GNS can prevent the covalent bonding between graphene and the substrate,[85−88] which guarantees the high quality of the prepared GNS-FETs. In addition, there are still several issues that need to be solved for the practical application of GNS-FET, for example the contact of GNS with electrodes and dielectrics, charge transport between GNS and electrodes, protection of GNS from the adsorption of any unwanted adsorbates, the integration of the connections, and so on.

CONCLUSION

In summary, the electronic structure and kinetic stability of GNS in graphane have been systematically studied by ab initio simulations. The band gap of Arm-GNS is determined by the spatial confinement of electrons, and modified by the contraction of the edge C−C bonds. The band gaps of all the three families ($N_A^C = 3p$, $3p + 1$, and $3p + 2$) of Arm-GNSs decrease inversely with increasing the width. The long-range nature of π electrons, spatial confinement, intraedge exchange interaction, and interedge superexchange interaction of electrons are essential factors to understand the band gap and magnetism of Zig-GNS, which are well explained by simple theoretical models. Furthermore, the kinetic simulations show that GNSs in graphane are very stable under conventional thermalization conditions. The hydrogen adatoms in the graphane bulk are much more stable than those at the graphene/graphane interface, which indicates that the desorption of adatoms will start at the interface if the system is placed under some kind of excitation. Thus, it is possible to carve out sharp-edge GNSs in graphane. We have proposed an approach based on SPM lithography to prepare integrated high-quality GNS-FETs, which is substrate-decoupled and robust under conventional thermalization conditions. This research should shed light on the electronic and kinetic properties of GNSs carved in other functionalized graphene (e.g., fluorographene[89,90]),[91,92] and be helpful for the engineering of graphene-based devices with desired structures and properties.

ASSOCIATED CONTENT

Supporting Information. Various relaxed supercells and the corresponding k grids for the density-functional simulations of electronic structure and reaction-path searching, some additional information on the band structures of GNS, the formulas for the jump frequencies of some chosen reaction paths for hydrogen adatoms at the graphene/graphane interface, and the

zero-point energy corrections to the potential barriers. This material is available free of charge via the Internet at http://pubs.acs.org/.

AUTHOR INFORMATION

Corresponding Author
*E-mail: lfhuang@theory.issp.ac.cn; zzeng@theory.issp.ac.cn.

ACKNOWLEDGMENT

The first author (Huang) wishes to thank An-ping Li from Oak Ridge National Laboratory, Chao Zhang from University of Wollongong, and some of his colleagues, Hao Ming Guo, Ling Ling Song, Yong Gang Li, Wang Huai Zhou, Xiao Li Zhang, Wei Fan, Shu Hui Zhang, and Hua Hao for helpful discussions. This work is supported by the National Science Foundation of China under Grant No. 10904148, the special Funds for Major State Basic Research Project of China(973) under Grant No. 2007CB925004973, Knowledge Innovation Program of the Chinese Academy of Sciences, and Director Grants of CASHIPS. Part of the calculations were performed at the Center for Computational Science of CASHIPS.

REFERENCES

(1) Novoselov, K. S.; Geim, A. K.; Morozov, S. V.; Jiang, D.; Zhang, Y.; Dubonos, S. V.; Grigorieva, I. V.; Firsov, A. A. *Science* **2004**, *306*, 666–669.
(2) Geim, A. K.; Novoselov, K. S. *Nat. Mater.* **2007**, *6*, 183–191.
(3) Katsnelson, M. I. *Mater. Today* **2007**, *10*, 20–27.
(4) Schwierz, F. *Nat. Nanotechnol.* **2010**, *5*, 487–496.
(5) Wei, D. C.; Liu, Y. Q. *Adv. Mater.* **2010**, *22*, 3225–3241.
(6) Yazyev, O. V. *Rep. Prog. Phys.* **2010**, *73*, 056501.
(7) Chen, C. Y.; Rosenblatt, S.; Bolotin, K. I.; Kalb, W.; Kim, P.; Kymissis, I.; Stormer, H. L.; Heinz, T. F.; Hone, J. *Nat. Nanotechnol.* **2009**, *4*, 861–867.
(8) Sluiter, M. H. F.; Kawazoe, Y. *Phys. Rev. B* **2003**, *68*, 085410.
(9) Elias, D. C.; Nair, R. R.; Mohiuddin, T. M. G.; Morozov, S. V.; Blake, P.; Halsall, M. P.; Ferrari, A. C.; Boukhvalov, D. W.; Katsnelson, M. I.; Geim, A. K.; Novoselov, K. S. *Science* **2009**, *323*, 610–613.
(10) Sofo, J. O.; Chaudhari, A. S.; Barber, G. D. *Phys. Rev. B* **2007**, *75*, 153401.
(11) Lebègue, S.; Klintenberg, M.; Eriksson, O.; Katsnelson, M. I. *Phys. Rev. B* **2009**, 245117.
(12) Leenaerts, O.; Peelaers, H.; Hernández-Nieves, A. D.; Partoens, B.; Peeters, F. M. *Phys. Rev. B* **2010**, *82*, 195436.
(13) Gao, H.; Wang, L.; Zhao, J.; Ding, F.; Lu, J. *J. Phys. Chem. C* **2011**, *115*, 3236–3242.
(14) Singh, A. K.; Yakobson, B. I. *Nano Lett.* **2009**, *9*, 1540–1543.
(15) Chernozatonskii, L. A.; Sorokin, P. B.; Brüning, J. W. *Appl. Phys. Lett.* **2007**, *91*, 183103.
(16) Chernozatonskii, L. A.; Sorokin, P. B. *J. Phys. Chem. C* **2010**, *114*, 3225–3229.
(17) Lee, J. H.; Grossman, J. C. *Appl. Phys. Lett.* **2010**, *97*, 133102.
(18) Wang, Z. F.; Zhang, Y.; Liu, F. *Phys. Rev. B* **2011**, *83*, R041403.
(19) Averill, F. W.; Morris, J. R. *Phys. Rev. B* **2011**, *84*, 035411.
(20) Reddy, C. D.; Cheng, Q. H.; Shenoy, V. B.; Zhang, Y. W. *J. Appl. Phys.* **2011**, *109*, 054314.
(21) Tozzini, V.; Pellegrini, V. *Phys. Rev. B* **2010**, *81*, 113404.
(22) Hernández-Nieves, A. D.; Partoens, B.; Peeters, F. M. *Phys. Rev. B* **2010**, *82*, 165412.
(23) Chen, Z.; Lin, Y. M.; Rooks, M. J.; Avouris, P. *Physica E* **2007**, *40*, 228–232.
(24) Han, M. Y.; Özyilmaz, B.; Zhang, Y. B.; Kim, P. *Phys. Rev. Lett.* **2007**, *98*, 206805.
(25) Li, X. L.; Wang, X. R.; Zhang, L.; Lee, S.; Dai, H. J. *Science* **2008**, *319*, 1229.
(26) Campos, L. C.; Manfrinato, V. R.; Sanchez-Yamagish, J. D.; Kong, J.; Jarilo-Herrero, P. *Nano Lett.* **2009**, *9*, 2600–2604.
(27) Jiao, L.; Wang, X. R.; Diankov, G.; Wang, H. L.; Dai, H. J. *Nat. Nanotechnol.* **2010**, *5*, 321–325.
(28) Shimizu, T.; Haruyama, J.; Marcano, D. C.; Kosinkin, D. V.; Tour, J. M.; Hirose, K.; Suenaga, K. *Nat. Nanotechnol.* **2010**, *6*, 45–50.
(29) Cai, J. M.; Ruffieux, P.; Jaafar, R.; Bieri, M.; Braun, T.; Blankenburg, S.; Muoth, M.; Seitsonen, A. P.; Saleh, M.; Feng, X.; Müllen, K.; Fasel, R. *Nature* **2010**, *466*, 470–473.
(30) Son, Y. W.; Cohen, M. L.; Louie, S. G. *Phys. Rev. Lett.* **2006**, *97*, 216803.
(31) Son, Y. W.; Cohen, M. L.; Louie, S. G. *Nature* **2006**, *444*, 347–349.
(32) Obradovic, B.; Kotlyar, R.; Heinz, F.; Matagne, P.; Rakshit, T.; Giles, M. D.; Stettler, M. A. *Appl. Phys. Lett.* **2006**, *88*, 142102.
(33) Barone, V.; Hod, O.; Scuseria, G. E. *Nano Lett.* **2006**, *6*, 2748–2754.
(34) Yang, L.; Park, C. H.; Son, Y. W.; Cohen, M. L.; Louie, S. G. *Phys. Rev. Lett.* **2007**, *99*, 186801.
(35) Zheng, W.; Sun, C. Q. *Energy Environ. Sci.* **2011**, *4*, 627–655.
(36) Wang, X. R.; Ouyang, Y. J.; Li, X. L.; Wang, H. L.; Guo, J.; Dai, H. J. *Phys. Rev. Lett.* **2008**, *100*, 206803.
(37) Kim, W. Y.; Kim, A. K. S. *Nat. Nanotechnol.* **2008**, *3*, 408–412.
(38) Bai, J.; Cheng, R.; Xiu, F.; Liao, L.; Wang, M.; Shailos, A.; Wang, K. L.; Huang, Y.; Duan, X. *Nat. Nanotechnol.* **2010**, *5*, 655–659.
(39) Flores, M. Z. S.; Autreto, P. A. S.; Legoas, S. B.; Galvao, D. S. *Nanotechnology* **2009**, *20*, 465704.
(40) Sessi, P.; Guest, J. R.; Bode, M.; Guisinger, N. P. *Nano Lett.* **2009**, *9*, 4343–4347.
(41) Zecho, T.; Güttler, A.; Sha, X.; Jackson, B.; Küppers, J. *J. Chem. Phys.* **2002**, *117*, 8488–8492.
(42) Zecho, T.; Güttler, A.; Sha, X.; Lemoine, D.; Jackson, B.; Küppers, J. *Chem. Phys. Lett.* **2002**, *366*, 188–195.
(43) Zecho, T.; Güttler, A.; Küppers, J. *Carbon* **2004**, *42*, 609–617.
(44) Hornekær, L.; Rauls, E.; Xu, W.; Šljivančanin, Ž.; Otero, R.; Stensgaard, I.; Lægsgaard, E.; Hammer, B.; Besenbacher, F. *Phys. Rev. Lett.* **2006**, *97*, 186102.
(45) Cuppen, H. M.; Hornekær, L. *J. Chem. Phys.* **2008**, *128*, 174707.
(46) Thomas, C.; Angot, T.; Layet, J. M. *Surf. Sci.* **2008**, *602*, 2311–2314.
(47) Huang, L. F.; Ni, M. Y.; Li, Y. G.; Zhou, W. H.; Zheng, X. H.; Guo, L. J.; Zeng, Z. *Surf. Sci.* **2011**, *605*, 1489–1496.
(48) Giannozzi, P.; Baroni, S.; Bonini, N.; Calandra, M.; Car, R.; Cavazzoni, C.; Ceresoli, D.; Chiarotti, G. L.; Cococcioni, M.; Dabo, I.; et al. *J. Phys.: Condens. Matter* **2009**, *21*, 395502.
(49) Vanderbilt, D. *Phys. Rev. B* **1990**, *41*, 7892.
(50) Perdew, J. P.; Burke, K.; Ernzerhof, M. *Phys. Rev. Lett.* **1996**, *77*, 3865.
(51) Henkelman, G.; Uberuage, B. P.; Jónsson, H. *J. Chem. Phys.* **2000**, *113*, 9901.
(52) Huang, L. F.; Ni, M. Y.; Zheng, X. H.; Zhou, W. H.; Li, Y. G.; Zeng, Z. *J. Phys. Chem. C* **2010**, *114*, 22636–22643.
(53) Kharche, N.; Zhou, Y.; O'Brien, K. P.; Kar, S.; Nayak, S. K. *ACS Nano* **2011**, *5*, 6096–6101.
(54) Huang, L. F.; Ni, M. Y.; Zhang, G. R.; Zhou, W. H.; Li, Y. G.; Zheng, X. H.; Zeng, Z. *J. Chem. Phys.* **2011**, *135*, 064705.
(55) Chan, M. K. Y.; Ceder, G. *Phys. Rev. Lett.* **2010**, *105*, 196403.
(56) Nakada, K.; Fujita, M. *Phys. Rev. B* **1996**, *54*, 17954–17961.
(57) Fujita, M.; Wakabayashi, K.; Nakada, K.; Kusakabe, K. *J. Phys. Soc. Jpn.* **1996**, *65*, 1920–1923.
(58) Pisani, L.; Chan, J. A.; Montanari, B.; Harrison, N. M. *Phys. Rev. B* **2007**, *75*, 064418.
(59) Yazyev, O. V.; Katsnelson, M. I. *Phys. Rev. Lett.* **2008**, *100*, 047209.
(60) Landau, L. D.; Lifshitz, E. M. *Quantum Mechanics (Non-relativistic Theory)*, 3rd ed.; Butterworth-Heinemann: Oxford, 1999; Chapter 7.

(61) Van Schilfgaarde, M.; Katsnelson, M. I. *Phys. Rev. B* **2011**, *83*, R081409.
(62) Ruffieux, P.; Cröning, O.; Schwaller, P.; Schlapbach, L.; Gröning, P. *Phys. Rev. Lett.* **2000**, *84*, 4910.
(63) Pisani, L.; Montanari, B.; Harrison, N. M. *New J. Phys.* **2008**, *10*, 033002.
(64) Casolo, S.; Lovvik, O. M.; Martinazzo, R.; Tantardini, G. F. *J. Chem. Phys.* **2009**, *130*, 054704.
(65) Wassmann, T.; Seitsonen, A. P.; Saitta, A. M.; Lazzeri, M.; Mauri, F. *J. Am. Chem. Soc.* **2010**, *132*, 3440–3451.
(66) Tao, C.; Jiao, L.; Yazyev, O. V.; Chen, Y. C.; Feng, J.; Zhang, X.; Capaz, R. B.; Tour, J. M.; Zettl, A.; Louie, S. G.; Dai, H.; Crommie, M. F. *Nat. Phys.* **2011**, *7*, 616–620.
(67) Zheng, X. H.; Wang, X. L.; Abtew, T. A.; Zeng, Z. *J. Phys. Chem. C* **2010**, *114*, 4190–4193.
(68) Martins, T. B.; Miwa, R. H.; da Silva, A. J. R.; Fazzio, A. *Phys. Rev. Lett.* **2007**, *98*, 196803.
(69) Zheng, X. H.; Rungger, I.; Zeng, Z.; Sanvito, S. *Phys. Rev. B* **2009**, *80*, 235426.
(70) Rudberg, E.; Salek, P.; Luo, Y. *Nano Lett.* **2007**, *7*, 2211–2213.
(71) Kan, E.; Li, Z.; Yang, J.; Hou, J. G. *Appl. Phys. Lett.* **2007**, *91*, 243116.
(72) Openov, L. A.; Podlivaev, A. I. *JETP Lett.* **2009**, *90*, 459–463.
(73) Ao, Z. M.; Nernández-Nieves, A. D.; Peeters, F. M.; Li, S. *Appl. Phys. Lett.* **2010**, *97*, 233109.
(74) Park, S.; Srivastava, D.; Cho, K. *Nano Lett.* **2003**, *3*, 1273–1277.
(75) Nikitin, A.; Zhang, Z.; Nilsson, A. *Nano Lett.* **2009**, *9*, 1301–1306.
(76) Bobrov, K.; Mayne, A. J.; Hoffman, A.; Dujardin, G. *Surf. Sci.* **2003**, *528*, 138–143.
(77) Tseng, A. A.; Notargiacomo, A.; Chen, T. P. *J. Vac. Sci. Technol., B* **2005**, *23*, 877–894.
(78) Jones, J. D.; Hoffmann, W. D.; Jesseph, A. V.; Morris, C. J.; Verbeck, G. F.; Perez, J. M. *Appl. Phys. Lett.* **2010**, *97*, 233104.
(79) Huang, R. Z.; Stepanyuk, V. S.; Kirschner, J. *J. Phys.: Condens. Matter* **2006**, *18*, L217–L223.
(80) Zhou, J.; Wang, Q.; Sun, Q.; Jena, P.; Chen, X. S. *Proc. Natl. Acad. Sci. U.S.A.* **2010**, *107*, 2801–2806.
(81) Penev, E.; Kratzer, P.; Scheffler, M. *J. Chem. Phys.* **1999**, *110*, 3986–3994.
(82) Petrini, D.; Larsson, K. *J. Phys. Chem. C* **2007**, *111*, 795–801.
(83) Peng, X.; Krüger, P.; Pollmann, J. *New J. Phys.* **2008**, *10*, 125028.
(84) King, S. W.; Davis, R. F.; Nemanich, R. J. *Surf. Sci.* **2009**, *603*, 3104–3118.
(85) Sque, S. J.; Jones, R. *Phys. Rev. B* **2007**, *75*, 115328.
(86) Riedl, C.; Coletti, C.; Iwasaki, T.; Zakharov, A. A.; Starke, U. *Phys. Rev. Lett.* **2009**, *103*, 246804.
(87) Lee, B.; Han, S.; Kim, Y. *Phys. Rev. B* **2010**, *81*, 075432.
(88) Hiebel, F.; Mallet, P.; Veuillen, J. Y.; Magaud, L. *Phys. Rev. B* **2011**, *83*, 075438.
(89) Nair, R. R.; et al. *Small* **2010**, *6*, 2877–2884.
(90) Jeon, K. J.; Lee, Z.; Pollak, E.; Moreschini, L.; Bostwick, A.; Park, C. M.; Mendelsberg, R.; Radmilovic, V.; Kostecki, R.; Richardson, T. J.; Rotenberg, E. *ACS Nano* **2011**, *5*, 1042–1046.
(91) Shen, N.; Sofo, J. O. *Phys. Rev. B* **2011**, *83*, 245424.
(92) Tang, S.; Zhang, S. *J. Phys. Chem. C* **2011**, *115*, 16644–16651.